Article:

Adetona, A.J., Wang, G. orcid.org/0000-0003-1842-8067, Walkley, B. orcid.org/0000-0003-1069-1362 et al. (2 more authors) (2024) Effect of ZrO2 stoichiometry on the structural and electrical properties of Na3Zr2−xSi2PO12-2x solid electrolyte. Journal of the European Ceramic Society, 44 (5). pp. 2989-2997. ISSN 0955-2219

https://doi.org/10.1016/j.jeurceramsoc.2023.12.071

Journal of the European Ceramic Society xxx (xxxx) xxx

Contents lists available at ScienceDirect

Journal of the European Ceramic Society

journal homepage: www.elsevier.com/locate/jeurceramsoc

Effect of ZrO_2 stoichiometry on the structural and electrical properties of $Na_3Zr_{2-x}Si_2PO_{12\text{-}2x}$ solid electrolyte

Ademola J. Adetona [a,*], Ge Wang [b], Brant Walkley [c], Derek C. Sinclair [a], Ian M. Reaney [a]

[a] *Department of Materials Science and Engineering, University of Sheffield, Sheffield S1 3JD, UK*
[b] *Department of Materials, University of Manchester, Sheffield M13 9PL, UK*
[c] *Department of Biological and Chemical Engineering, University of Sheffield, Sheffield S1 3JD, UK*

ARTICLE INFO

Keywords:
NASICON
Solid electrolyte
Solid-state method
Scanning electron microscopy
Electrochemical Impedance Spectroscopy

ABSTRACT

$Na_3Zr_2Si_2P_2O_{12}$ (NZSP) has potential use as a solid electrolyte in Na-ion solid-state batteries due to its high ionic conductivity (10^{-3}–10^{-4} Scm^{-1}) at room temperature. It is established that all previous preparations involving the solid-state method for NZSP compositions contain *m*-ZrO_2 as a secondary phase. Here, the solid-state method is used to prepare single-phase NZSP by modifying the mole fractions of the ZrO_2 reactant. Reducing ZrO_2 concentration may also create Zr and O vacancies and potentially increase the hopping sites for Na-ion conduction. X-ray diffraction, scanning electron microscopy, Raman and Fourier Transform Infrared spectroscopy, dilatometry and impedance spectroscopy were used to characterise the structure, morphology and electrical properties of single-phase NZSP, and the results were compared with samples that have *m*-ZrO_2 secondary phase ($Na_3Zr_2Si_2PO_{12}$). The role of *m*-ZrO_2 impurities on the conductivity of NZSP is investigated and compared with available literature.

1. Introduction

The current global energy production and distribution crisis has demonstrated that our reliance on fossil fuels damages the environment and is also subjected to geopolitical uncertainty [1,2]. Therefore, the current energy crisis has made world leaders focus even more acutely on developing a secure and sustainable strategy for generating power and reducing dependence on fossil fuels. Since Sony Corporation commercialised Li-ion batteries (LIBs) in 1991 [3,4], there has been a surge in demand. However, conventional LIBs face challenges of low retention [5], dendrite formation [6], leakage [7], combustion [8], low battery life cycle and increased manufacturing costs due to the limited availability of Li-ion precursors [5–9].

Na-ion batteries (NIBs) are considered viable alternatives to LIBs due to the abundance of Na-ion precursors [10] and their similarity in function. However, NIBs face similar challenges to LIBs. Sodium-ion solid-state batteries (SSSBs) hold great potential as an alternative to traditional LIBs or NIBs. Solid-state batteries (SSBs) utilise a solid electrolyte instead of a liquid or gel-like electrolyte found in Li-ion and Na-ion batteries [11]. One of the advantages of exploring SSSBs is the abundance and affordability of sodium precursors [12]. Lithium resources are limited and concentrated in a few regions, making LIBs expensive, but sodium precursors are widely available, and their production costs are cheaper [3,13]. Therefore, SSSBs may offer a cost-effective, safer and more sustainable energy storage solution, especially for large-scale applications [14]. Solid electrolytes (SEs) eliminate the risk of leakage, degradation and thermal runaway associated with liquid electrolytes [15–17]. The enhanced safety makes SSBs highly desirable for various applications, including consumer electronics, electric vehicles and grid energy storage [18–25].

Various solid electrolytes (SEs), such as ceramics, glasses, and polymeric materials, have been explored to improve battery performance and reduce the interfacial resistance between electrodes and electrolytes [26–30]. Oxide-based solid electrolytes have been extensively studied for their ease of preparation, stability, fast-ion conduction, non-flammability, ion mobility and potential applications in batteries and advanced energy storage devices [31–37]. NASICON is an acronym for Sodium Super Ionic Conductors, an oxide-based inorganic SE with the general formula $A_xM_2(PO_4)_3$ [38]. The “A-site” is usually occupied by mobile monovalent ions such as Na^+ or Li^+. “x” is the

---

* Corresponding author.
E-mail address: adetonaademola077@gmail.com (A.J. Adetona).

https://doi.org/10.1016/j.jeurceramsoc.2023.12.071
Received 26 July 2023; Received in revised form 13 December 2023; Accepted 18 December 2023

Please cite this article as: Ademola J. Adetona et al., *Journal of the European Ceramic Society*, https://doi.org/10.1016/j.jeurceramsoc.2023.12.071

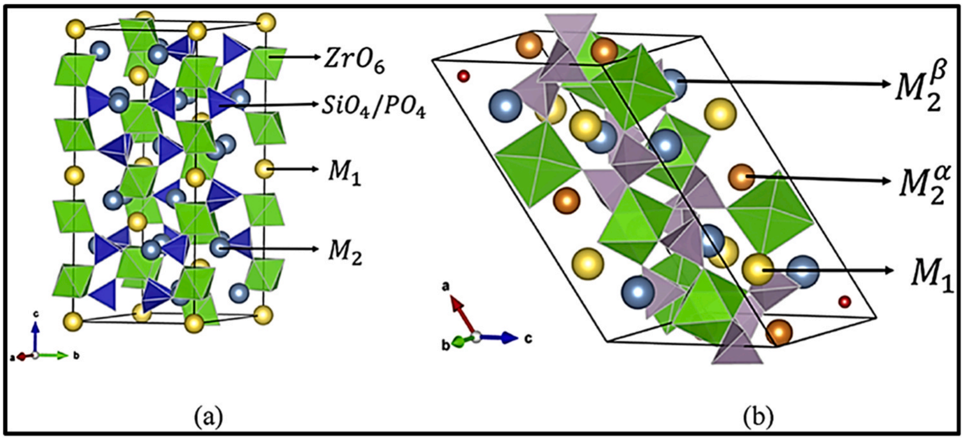

Fig. 1. Unit cells of $Na_{1+x}Zr_2Si_xP_{3-x}O_{12}$ solid electrolyte: (a) rhombohedral structure with two Na^+ sites (M_1 and M_2) and (b) monoclinic structure with three Na^+ sites, the M_2 sites split into M_2^α and M_2^β [44].

Table 1
Preparation methods, sintering temperature, time, crystal structure and room temperature conductivity of NZSP.

NASICON	Preparation methods	Sintering Temp. (°C)	Time (Hours)	Crystal structure	Ionic conductivity (S/cm)	Ref.
$Na_{3.05}Zr_2Si_{2.05}P_{0.95}O_{12}$	Sol-gel	1000	3	Rhombohedral	2.01×10^{-4}	[45]
$Na_{2.8}Zr_2Si_{1.8}P_{1.2}O_{12}$	Co-precipitation method	1175	5	Rhombohedral	-	[46]
$Na_3Zr_2Si_2PO_{12}$	Solid-state	1230	40	Monoclinic	1.16×10^{-3}	[47]
$Na_3Zr_2Si_2PO_{13}$	Solid-state	1250	5	Monoclinic	6.1×10^{-4}	[48]
$Na_3Zr_2Si_2PO_{12}$	Spark Plasma	1250	5	Monoclinic	1.8×10^{-3}	[49]
$Na_3Zr_2Si_2PO_{12}$	Tape casting	1100	4	Monoclinic	4.4×10^{-4}	[50]
$Na_3Zr_2(SiO_4)_2(PO_4)$	SA-SSR	1250	5	Monoclinic	1.03×10^{-3}	[51]
$Na_{3.256}Mg_{0.128}Zr_{1.872}Si_2PO_{12}$	Cold sintering (780 MPa)	140	2	Rhombohedral	5.0×10^{-4}	[52]
$Na_{3.256}Mg_{0.128}Zr_{1.872}Si_2PO_{12}$	Solid-state	1300	24	Monoclinic & Rhombohedral	2.7×10^{-3}	[53]

number of monovalent ions present in the system, and the "M-site" can be occupied by trivalent (Sc^{3+} and La^{3+}), tetravalent (Zr^{4+}, Ge^{4+}) and/or pentavalent (Ta^{5+}, V^{5+}) elements. The P-site is usually co-shared by Si and/or P. NZSP with the formula $Na_{1+x}Zr_2Si_xP_{3-x}O_{12}$ ($0.0 \leq x \leq 3.0$) has been extensively studied as a solid electrolyte for all SSSBs and solid ionic devices [38–41]. The ionic conductivity of NZSP depends on factors such as the Na^+ concentration, Na^+ mobility/diffusion and crystal symmetry [38]. In NZSP, Na^+ ions move through channels in the ZrO_6 octahedra and SiO_4/PO_4 tetrahedra structure. Two distinct crystal symmetries, monoclinic (*C12/c*) and rhombohedral (*R-3c*), are known for $Na_{1+x}Zr_2Si_xP_{3-x}O_{12}$ ($0.0 \leq x \leq 3.0$), Fig. 1. The monoclinic phase occurred between $1.8 \leq x \leq 2.2$ and was studied to be thermally stable at room temperature (RT) with conductivity between 10^{-3} - 10^{-4} S/cm [39]. However, crystal symmetry and DFT studies [38–40] demonstrated that the rhombohedral phase, which occurred at $x \geq 2.2$, is more symmetrically stable with a lower activation energy (E_a) for Na^+ ions diffusion [41–43]. Also, studies on the crystal symmetry of ZrO_2 reactants suggest that *c*-ZrO_2 (c = cubic) promotes the conductivity of NZSP and suppresses the formation of *m*-ZrO_2 (m = monoclinic) [48]. Table 1 presents various preparation methods (solid-state, sol-gel, solution-assisted solid-state reaction, tape casting, co-precipitation, spark plasma and cold-sintering), conditions (the sintering temperature and time, crystal structure and the RT ionic conductivity) doping techniques and reactants modification adopted to suppress the formation of *m*-ZrO_2 and Na_3PO_4 as secondary phases and enhance ionic conductivity of NZSP.

Our study adjusts the mole fractions of the ZrO_2 reactant, thereby creating vacancies in both the Zr and O sites of NZSP with a view to suppressing the *m*-ZrO_2 impurity phase and simultaneously increasing the ionic conductivity due to an increase in hopping vacancies. Scanning Electron Microscopy, Raman and FTIR spectroscopy were used to obtain microstructural and structural information, which was then used to interpret the ionic conductivity in comparison with scientific literature.

2. Experimental methods

2.1. Materials preparation

The solid-state reaction method was used to prepare different NZSP compositions according to the formula in Eq. 2.1. *m*-ZrO_2 (purity 99%, Sigma Aldrich) and Na_3PO_4 (purity 98%, Sigma Aldrich) were preheated at 1000 ℃ and 180 ℃, respectively, to remove gases and hydrates. and were reacted with SiO_2 (purity 99.5%, Sigma Aldrich).

$$(2\text{-}x)ZrO_2 + Na_3PO_4 + 2SiO_2 \rightarrow Na_3Zr_{2-x}Si_2PO_{12-2x} \qquad (2.1)$$

x represents the mole fractions of the compositional series (0.10, 0.20, 0.30, 0.40, 0.50 and 0.60) prepared. The mixtures were ball milled at 300 rpm for 12 h using zirconia milling media in isopropanol, then dried at 120 ℃ for 12 h. The dried mixtures were ground to form a fine powder and heated at 400 °C for 5 h to remove residue. The powders were pelletised and calcined for 12 h at 900 ℃, forming an amorphous NZSP mixture. The amorphous NZSP mixture was further ball-milled at

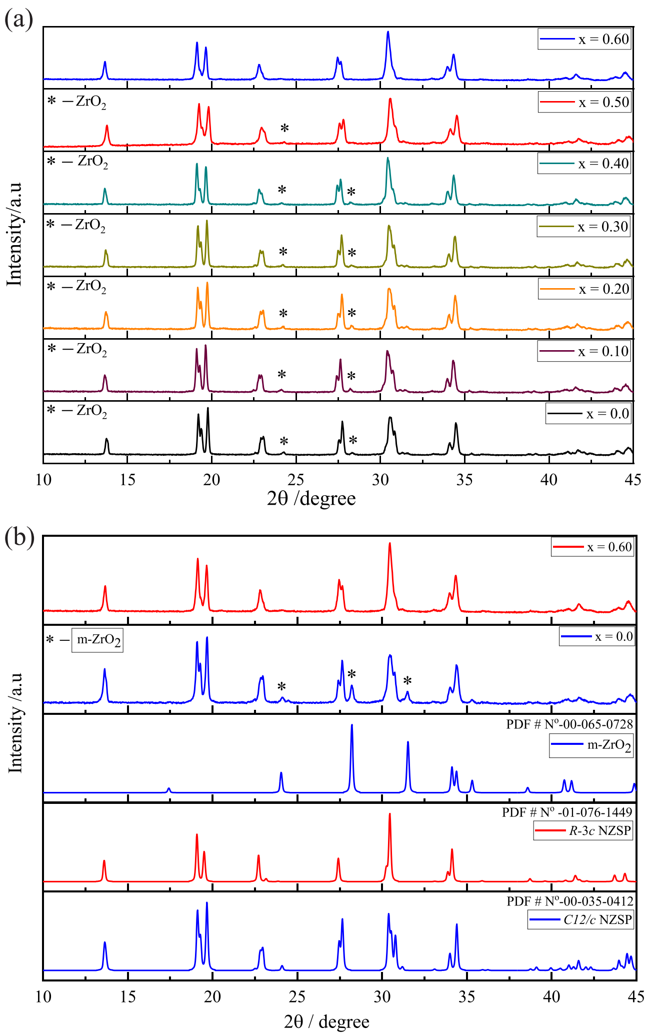

Fig. 2. (a) XRD patterns of $Na_3Zr_{2-x}Si_2PO_{12-2x}$ compositional series ($0.0 \leq x \leq 0.60$) with (*) depicting the ZrO_2 secondary phase. (b) XRD patterns matching the composition of $Na_3Zr_{2-x}Si_2PO_{12-2x}$ ($x = 0.0$ and 0.60) against the PDF card N° of monoclinic and rhombohedral NZSP and monoclinic ZrO_2.

300 rpm for 12 h and dried, and the powders were pelletised. The NZSP pellets were buried in green NZSP powder before being sintered at temperatures between 1100 - 1250 ℃ for 6 – 12 h.

2.2. Materials characterisations

The volume change of the green NZSP pellets as a function of temperature was studied using a Netzsch LFA hyper flash high-temperature dilatometer. The density of the sintered NZSP pellets was measured using Archimedes' method. A PANalytical Aeris X-ray diffractometer with Cu-Kα radiation (λ = 0.154 nm) in the 2θ range 10 – 45° and a step size of 0.02 was used to study the diffraction data of the sintered NZSP pellets. Phase refinement was performed on the diffraction data of NZSP ($x = 0.0$ and 0.60) using Topas 5 software. Vibrational spectra of the *m*-ZrO_2 and sintered NZSP ($x = 0.0$ and 0.60) were obtained using a Renishaw in-Via Raman microscope and a Perkin Elmer Frontier Fourier Transform Infrared spectroscopy. Microstructural studies were performed on the sintered pellets of NZSP ($x = 0.0$ and 0.60) using an FEI Inspect F Scanning electron microscopy.

Impedance spectroscopy was performed on the lightly polished surface of the sintered NZSP pellets ($x = 0.0$ and 0.60) with Au paste electrodes applied and fired at 850 °C for 2 h. Impedance spectroscopy (EIS) was performed using an Agilent 4294 A from RT to 800 °C at intervals of 50 °C and an Oxford Instrument CCC1104 closed cycle cooler Cryostat from 140 to 295 K at an interval of 20 K. Impedance data were normalised by a geometric factor (thickness/electrode area), and the estimated resistivity was obtained using ZView software.

3. Results and discussion

3.1. X-ray diffraction

XRD patterns acquired from $Na_3Zr_{2-x}Si_2PO_{12-2x}$ ($0.0 \leq x \leq 0.6$) sintered at 1250 °C for 6 h are shown in Fig. 2a. Prior to choosing these densification conditions, various sintering temperatures (1100, 1200 and 1250 °C) were investigated, with the results shown in Fig. S1. The diffraction plots in Fig. 2a revealed the effect of decreasing the mole fractions of ZrO_2. $Na_3Zr_{2-x}Si_2PO_{12-2x}$ ($x = 0.0$, 0.10, 0.20, 0.30 and 0.40) exhibited a *m*-ZrO_2 impurity phase (* symbol) at 2θ degree value 24.27 and 28.30, similar to reported data [48–53] but for $x = 0.50$ and 0.60, *m*-ZrO_2 was either suppressed ($x = 0.50$) or absent ($x = 0.60$), Fig. 2a. NZSP ($x = 0.60$) was therefore further investigated and compared with NZSP ($x = 0.0$) and literature data.

In Fig. 2b, XRD peaks from NZSP ($x = 0.0$ and 0.60) are matched against data files from the International Centre for Diffraction Data (ICDD): *m*-ZrO_2 (PDF N° 00–065-0728) and monoclinic and rhombohedral NZSP (PDF N° 00–035-0412 and 01–076-1449, respectively). Most peaks for $x = 0.0$ matched monoclinic NZSP (PDF N° 00–035-0412) except those at 24.23 and 28.30 °2θ, which corresponded to *m*-ZrO_2 [46–53]. In contrast, most peaks in NZSP ($x = 0.60$) could be indexed according to rhombohedral NZSP symmetry with associated changes in peak height and shape at 19.87, 23.11 °2θ but with the peak at 27.96 °2θ matching monoclinic symmetry, Fig. 2b. Therefore, it was concluded that $Na_3Zr_{2-x}Si_2PO_{12-2x}$ ($x = 0.60$) was dominantly single-phase, rhombohedral NZSP within the detection limits of our in-house diffractometer.

Diffraction data of NZSP ($x = 0.0$ and 0.60) were analysed using a full-pattern Rietveld refinement method to gain further insight into the crystal structure and phase formation of NZSP compositions. Table 2 shows the lattice parameters, theoretical density, goodness of fit (GoF),

Table 2
Refined parameters, phase fractions, the goodness of fit (GoF), cell volume, theoretical and relative density of NZSP composition series. *R*-rhombohedral and *M*-monoclinic.

NZSP	Phase fraction (%)			Lattice parameters (Å)			β (°)	GoF	Unit cell volume	Theoretical density	Relative density (%)
	C12/c	*R-3c*	*m*-ZrO_2	a	b	c					
$x = 0.0$	92.00	0.00	8.00	15.634 ± 0.0063	9.043 ± 0.0050	9.230 ± 0.0025	123.63	2.50	1086.6	3.244	95.06
$x = 0.60$	*C12/c* 47.00	*R-3c* 53.00	0.00	9.072 (*R*) 15.651 (*M*)	9.055	23.138 (*R*) 9.219 (*M*)	123.77	2.12	1086.1	3.204	94.30

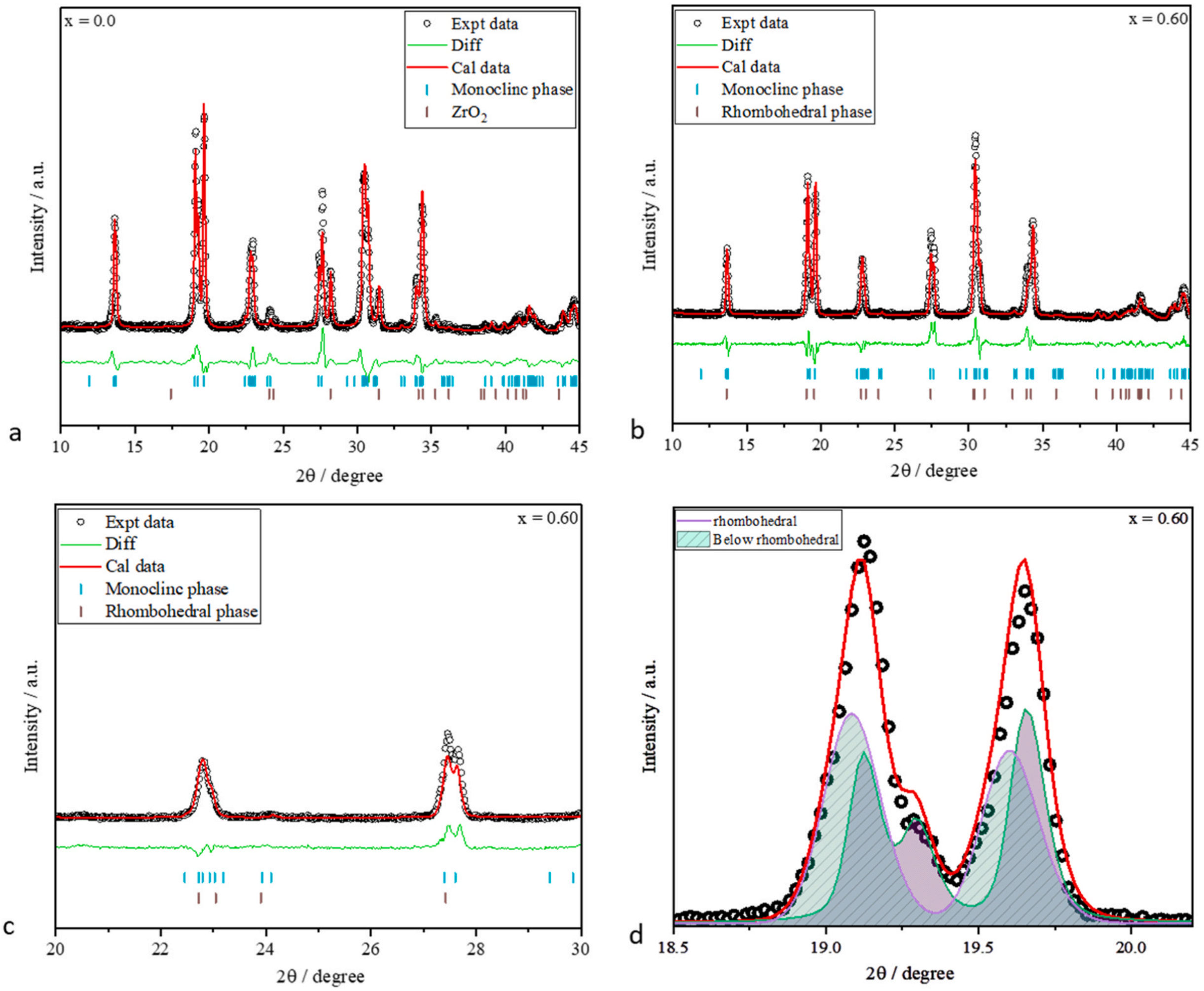

Fig. 3. (a-d). Full pattern Rietveld refinement of $Na_3Zr_{2-x}Si_2PO_{12-2x}$ (a) x = 0.0, (b) x = 0.60, (c) enlargement plot of x = 0.60 without impurity peaks, and (d) peaks representing the composition of rhombohedral and monoclinic phase in x = 0.60.

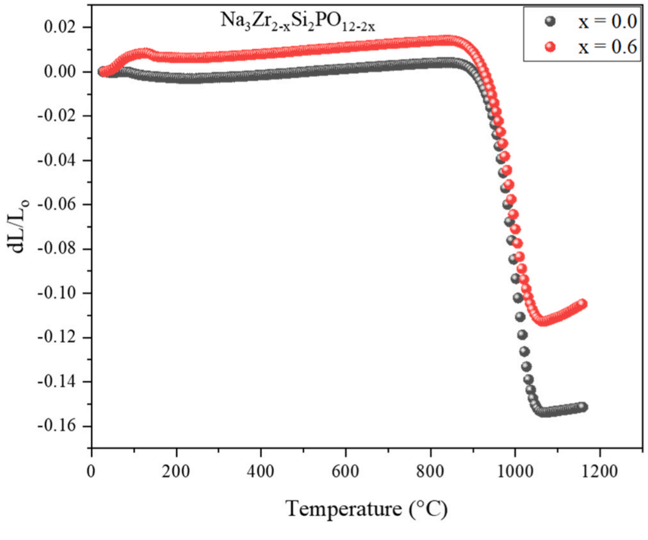

Fig. 4. Volume changes (shrinkage plots) of $Na_3Zr_{2-x}Si_2PO_{12-2x}$ (x = 0.0 & 0.60) against temperature.

unit cell volume and the percentage composition of the different phases. Fig. 3a reveals a 92% *m*-NZSP and an 8% *m*-ZrO_2 for NZSP (x = 0.0), consistent with the literature [48] with *a*, *b* and *c* values and GoF similar to those reported by refs. [48,53]. The refinement for NZSP (x = 0.60) confirms it is composed of two phases, 53% rhombohedral (*R-3c*) and 47% monoclinic (*C12/c*), with no evidence of *m*-ZrO_2 impurity phase, Fig. 3b, c and d. Tables S1–S3 show the full sets of refined parameters for NZSP (x = 0.0 and 0.60). The parameters for NZSP (x = 0.0) agree with those reported in the literature [48–53], but NZSP (x = 0.60) has not, to our knowledge, been previously prepared.

3.2. Relative density measurement

The densities of $Na_3Zr_{2-x}Si_2PO_{12-2x}$ (x = 0.0 and 0.60) sintered pellets were measured using Archimedes' method, and the results were compared with their theoretical density obtained from refinements. From our refinements, the theoretical density of NZSP (x = 0.0) is 3.24 gcm^{-3}, Table 2, which agrees with literature values [46–50]. The theoretical density of NZSP (x = 0.60) obtained from the XRD refinements is 3.20 gcm^{-3}, Table 2. The relative densities (ρ_r) of both NZSP (x = 0.0 and 0.60) were greater than 94%. The ρ_r and the sintering

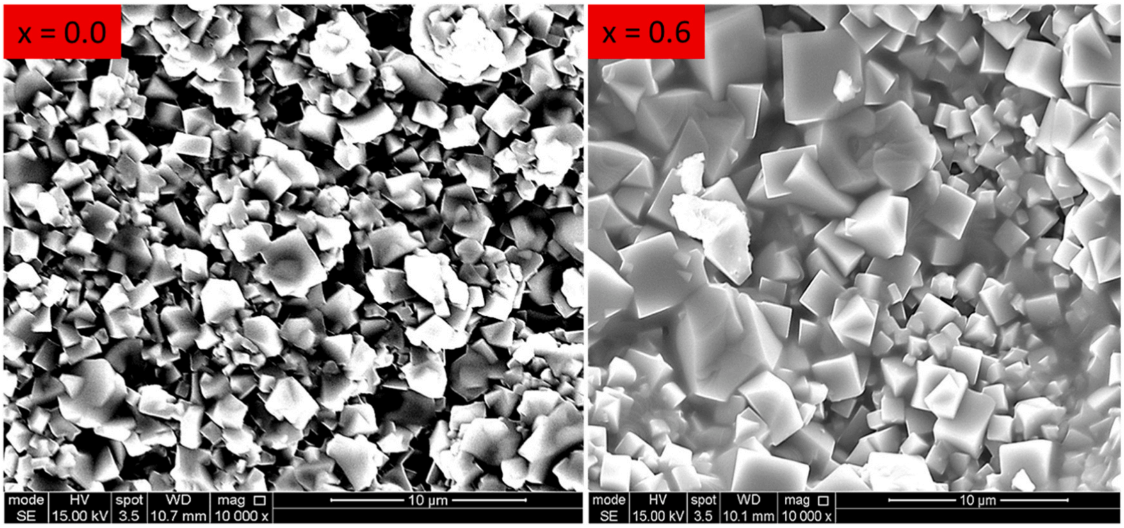

Fig. 5. The SEM fractured surface images of $Na_3Zr_{2-x}Si_2PO_{12-2x}$ (x = 0.0 and x = 0.60).

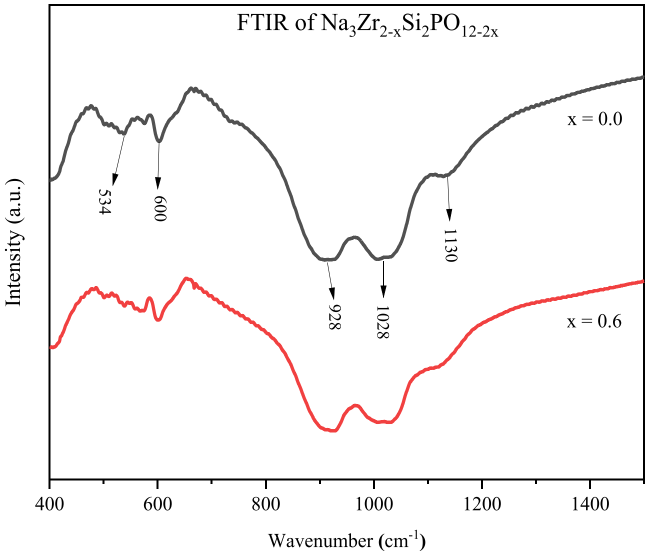

Fig. 6. FTIR spectra for $Na_3Zr_{2-x}Si_2PO_{12-2x}$ (x = 0.0 & 0.60).

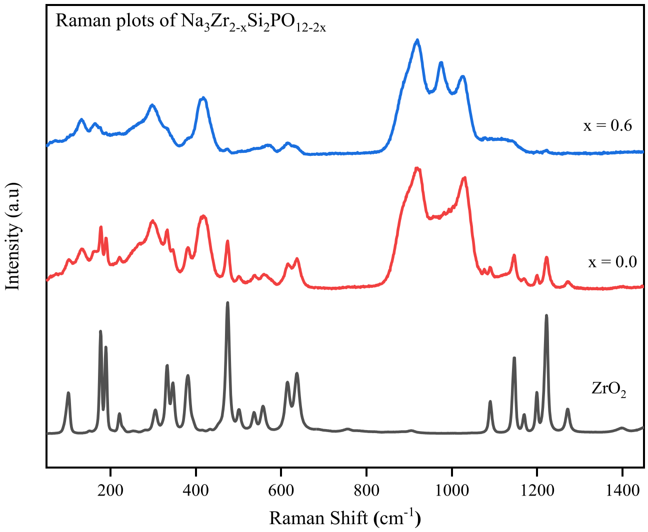

Fig. 7. Raman spectra of $Na_3Zr_{2-x}Si_2PO_{12-2x}$ (x = 0.0 & 0.60) and ZrO_2.

parameters are shown in Table S4 of the Supporting Information.

3.3. Dilatometry

The change in the volume of the green pellets as a function of the temperature of $Na_3Zr_{2-x}Si_2PO_{12-2x}$ (x = 0.0 and 0.60) is shown in the dilatometer plots in Fig. 4. The two compositions of the NZSP (x = 0.0 and 0.60) show similar volume contraction over a wide temperature range. The volume changes were measured between 0 and 1200 °C to investigate the 'melt pool phase' temperature in NZSP as observed by [53]. The 'melt pool phase' for the NZSP (x = 0.0 and 0.60) was observed to occur between 905 - 1086 °C, Fig. 4. This melt pool phase should not be confused with the sintering temperature of NZSP, which is ≥ 1200 °C. Regardless of the compositional changes in the mole fractions of the ZrO_2 reactant, the volume of the green pellets contracted similarly, consistent with their densities.

3.4. Scanning electron microscopy

SEM images of the fractured surface of the sintered pellets of $Na_3Zr_{2-x}Si_2PO_{12-2x}$ (x = 0.0 and x = 0.60) are shown in Fig. 5. The micrographs for both NZSP (x = 0.0 and 0.6) reveal micron-sized, cuboid and homogeneous grain structures that are well-sintered and tightly compacted, supporting Archimedes' density measurements and comparable to the literature [48,53]. The average grain size of the NZSP (x = 0.0) is ≤ 2 μm with few voids, consistent with a material of $\rho_r \sim$ 95%. The average grain size of NZSP (x = 0.60) is > 3 μm with few voids consistent with a ceramic of $\rho_r \sim$ 94%. Overall, the grain size of the NZSP (x = 0.60) is approximately 35% larger than that of NZSP (x = 0.0). *m*-ZrO_2 secondary phase was not visible in the micrograph for NZSP (x = 0.0) even though XRD and Raman spectroscopy (see later)

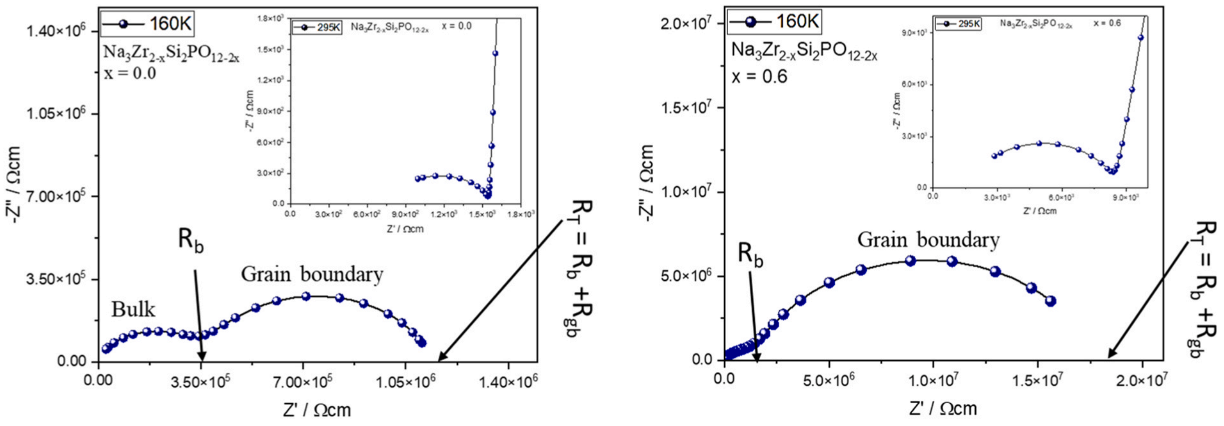

Fig. 8. The complex impedance plots of $Na_3Zr_{2-x}Si_2PO_{12-2x}$ (x = 0.0 and 0.60) at 160 and 295 K (insert) show the bulk and grain boundary conductions. [R_b: Bulk resistance, R_{gb}: Grain boundary resistance and R_T: Total resistance].

unambiguously demonstrate its presence. However, polished sections coupled with backscattered imaging may reveal the distribution of the *m*-ZrO_2 secondary phase. Additional SEM micrographs for NZSP (x = 0.0 & x = 0.60) are shown in Fig. S2.

3.5. *Fourier transform infra-red (FTIR) spectroscopy*

FTIR spectra of $Na_3Zr_{2-x}Si_2PO_{12-2x}$ (x = 0.0 and 0.60) are shown in Fig. 6. There were no observable differences in the vibrational and stretching frequencies between the two compositions of NZSP (x = 0.0 and 0.60). Transition metal-oxygen bonds have a unique fingerprint at < 1000 cm^{-1} with Zr-O stretching/vibration bands dominant in this region [54,55]. The Zr–O bond vibrational frequency occurs in the 400 – 600 cm^{-1} range. Thus, the peaks at 534 and 600 cm^{-1} in Fig. 6 can be attributed to the Zr–O bond. Similarly, the P–O bond vibrational frequency lies between 1100 – 1300 cm^{-1}; hence, the peak at 1130 cm^{-1} is assigned to the P–O bond. The Si–O bond has a unique signature between 900 – 1100 cm^{-1} and therefore, the modes at 928 and 1028 cm^{-1} are assigned to the Si–O bond. However, it is crucial to note that the vibrational frequency of M–O can vary based on the atoms involved, coordination environment, surrounding functional groups, and molecular structure. Hence, determining the vibrational frequency requires careful consideration of these factors.

3.6. *Raman spectroscopy*

Raman data of NZSP (x = 0.0 and 0.60) and *m*-ZrO_2 are shown in Fig. 7. The NZSP spectra are similar to those obtained for NASICON reported by Barj *et al.*, [55]. Based on the refinement of the X-ray diffraction data, it is reasonable to assume that all the peaks for NZSP (x = 0.60) in Fig. 7 arise only from the matrix phase with none matching *m*-ZrO_2, which supports our premise that this composition is a single phase. The peak at 960 cm^{-1} in NZSP (x = 0.60) does not match *m*-ZrO_2 and is absent in the monoclinic crystal symmetry of NZSP (x = 0.0) and likely relates to either rhombohedral symmetry or Zr-O site occupancy changes. Nonetheless, it requires further study. For NZSP (x = 0.0), all modes match either *m*-ZrO_2 or NZSP (x = 0.60), supporting the XRD data from NZSP (x = 0.0) in which peaks associated with *m*-ZrO_2 were observed.

3.7. *Impedance spectroscopy*

Complex impedance plane, Z * plots at various temperatures for $Na_3Zr_{2-x}Si_2PO_{12-2x}$ ceramics (x = 0.0 and 0.60) sintered at 1250 °C are shown in Fig. 8(a & b). A low-frequency spike and a partial arc with a non-zero intercept at high frequencies are observed at room temperature in Fig. 8(a & b) insert. However, the arc rapidly disappears at higher temperatures, and only a non-zero intercept on the Z′ axis of the spike was observed. The low-frequency spike is consistent with ionic conduction, with the charge carriers being Na^+ ions. Therefore, only the total resistivity of the ceramics could be obtained based on the intercept of the spike with the Z′ axis. However, the total resistivity of $Na_3Zr_{2-x}Si_2PO_{12-2x}$ (x = 0.0) is slightly lower than that of $Na_3Zr_{2-x}Si_2PO_{12-2x}$ (x = 0.60) at room and higher temperatures, and its order of magnitude agrees with reported literature [46–53]. An Arrhenius plot of the total conductivity of the ceramics (where $\sigma_T = 1/R_T$) is shown in Fig. 9(a), where the activation energy (E_a) is ~ 0.30 eV for both materials.

Sub-ambient measurements were performed to probe the electro-active contributions to the total conductivity. Z * plots for 160 K revealed both to display two arcs, Fig. 8. An equivalent circuit based on two parallel Resistor-Capacitor elements connected in series was used to interpret and quantify the sub-ambient impedance data. The high and low-frequency arcs had associated capacitance values in the range pF/cm and nF/cm, respectively and are therefore consistent with bulk (R_bC_b) and grain boundary ($R_{gb}C_{gb}$) responses, respectively. The contributions of the bulk, grain boundary and total resistivity at 160 and 295 K are shown in Table 3. Arrhenius plots of the bulk ($\sigma_b = 1/R_b$) and grain boundary ($\sigma_{gb} = 1/R_{gb}$) are shown in Fig. 9(b) and (c), respectively. E_a associated with σ_b is ~ 0.25 eV for both ceramics, and this indicates a similar conduction mechanism in both materials, with the difference in σ_b being attributed to a lower carrier concentration in x = 0.60. E_a associated with σ_{gb} is higher in both cases and is in the range ~ 0.30 – 0.35 eV, Fig. 9(c). These results are in good agreement with reported literature [48,53,56]. Figs. S3 and S4 show the relaxation frequency of the impedance plots.

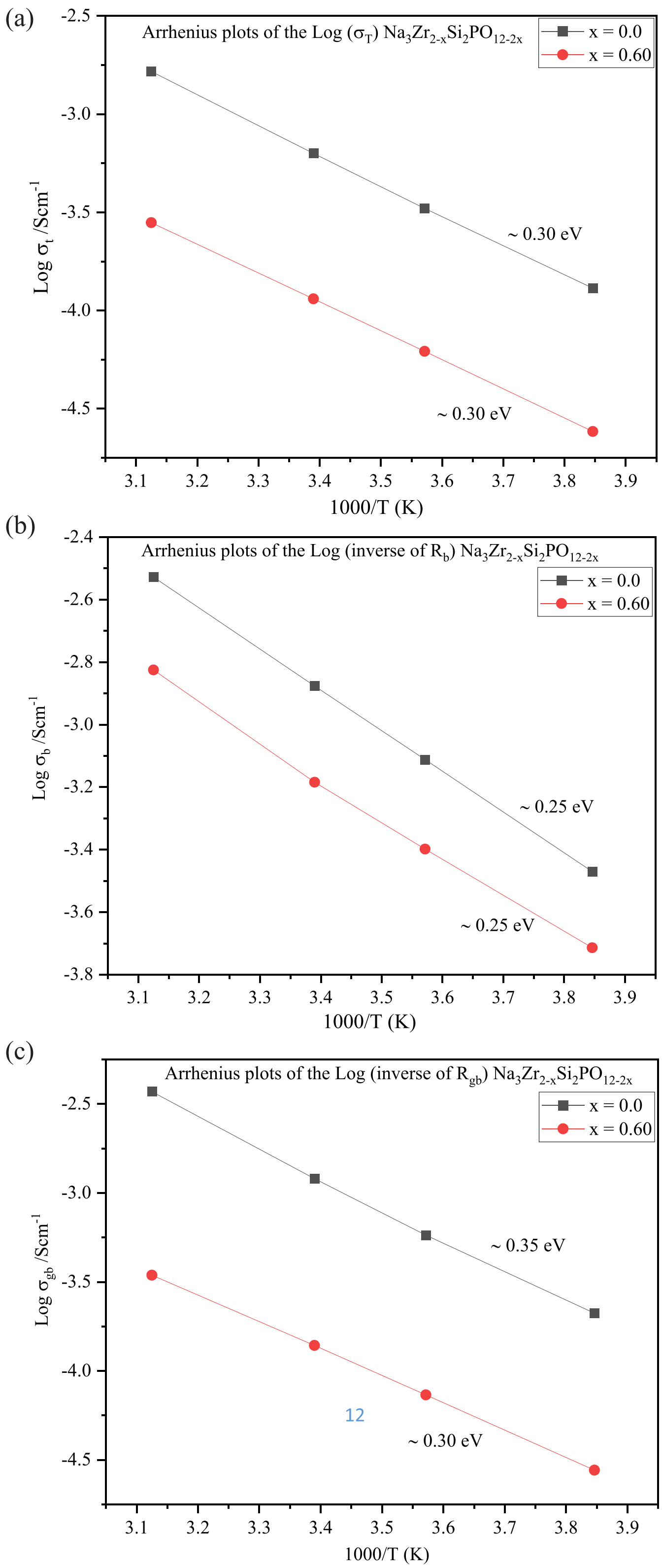

Fig. 9. a. Arrhenius plots of the total conductivity for NZSP (x = 0.0 and 0.60) ceramics. (b). Temperature-dependent bulk conductivity (σ_b) plots of NZSP (x = 0.0 and 0.60). (c). Temperature-dependent grain boundary conductivity (σ_{gb}) plots of NZSP (x = 0.0 and 0.60).

4. Conclusions

The NASICON, $Na_{x+1}Zr_2Si_xP_{3-x}O_{12}$ ($0.0 \leq x \leq 3.0$) has been widely studied, but researchers have not to date been able to prepare single-phase with compositions containing ZrO_2 secondary phase. Several compositions of NZSP with varying mole fractions of ZrO_2 reactant were prepared. $Na_3Zr_{2-x}Si_2PO_{12-2x}$ (x = 0.60) resulted in mixed rhombohedral and monoclinic crystal phases but with the absence of *m*-ZrO_2 impurities. Refinement of XRD data confirmed the presence of mixed monoclinic (*C12/c*) and rhombohedral (*R-3c*) phases for x = 0.60. Raman spectroscopy and XRD confirmed a single-phase $Na_3Zr_{2-x}Si_2PO_{12-2x}$ (x = 0.60) and the presence of *m*-ZrO_2 in all other compositions. SEM images revealed a dense, cuboid grain morphology for both compositions (x = 0.0 and 0.60) typical of NASICONs. The bulk, grain boundary and total ionic conductivity of the NZSP (x = 0.0 and 0.60) were investigated at 293 K and 160 K using impedance spectroscopy. With a monoclinic crystal structure, NZSP (x = 0.0) has a higher RT bulk conductivity of $\sim 1.3 * 10^{-3}$ Scm^{-1}. In contrast, NZSP (x = 0.60) with mixed rhombohedral and monoclinic crystal structures gave a slightly lower RT bulk conductivity of $\sim 6.5 * 10^{-4}$ Scm^{-1}, but both were comparable with literature values.

CRediT authorship contribution statement

Ademola Adetona: **Conceptualization**: The primary ideas and research question were conceived by the author. **Methodology**: The author developed the research design, collected and analyzed the data. **Investigation**: The author conducted experiments and gathered relevant data. **Writing - Original Draft**: The author wrote the initial draft of the manuscript. **Writing - Review & Editing**: The author contributed to the revision and editing process. **Visualization**: The author created the figures and visual elements used in the manuscript. **Validation**: The author verified the accuracy and integrity of the research findings. **Funding Acquisition**: The author secured financial support for the project. **Project Administration**: The author managed the project and ensured its smooth execution. Ge Wang: **Supervision**: The author supervised the research project. **Writing - Review & Editing**: The author provided critical feedback and contributed to the improvement of the manuscript. **Validation**: The author verified the accuracy and integrity of the research findings. Brant Walkley: **Supervision**: The author supervised the research project. **Writing - Review & Editing**: The author provided critical feedback and contributed to the improvement of the manuscript. Derek Sinclair: **Supervision**: The author supervised the Impedance spectroscopy aspect of the research project. **Methodology**: The author analyzed the data. **Writing - Review & Editing**: The author provided critical feedback and contributed to the improvement of the manuscript. **Validation**: The author verified the accuracy and integrity of the research findings. Ian Reaney: **Conceptualization**: The primary ideas and research question were conceived by the author. **Supervision**: The author supervised and coordinated the overall research project. **Methodology**: The author developed the research design, collected and analyzed the data. **Writing - Review & Editing**: The author provided critical feedback and contributed to the improvement of the manuscript. **Project Administration**: The author managed the project and ensured its smooth execution. **Validation**: The author verified the accuracy and integrity of the research findings.

Declaration of Competing Interest

The authors declare no known competing financial interests that could have influenced the work reported in this paper.

Table 3
The bulk and grain boundary capacitance at 160 K and the bulk, grain boundary and total ionic conductivities of the $Na_3Zr_{2-x}Si_2PO_{12-2x}$ (x = 0.0 & 0.60) ceramic at 160 and 295 K.

NZSP	Capacitance (F/cm) = $1/2\pi f_{max}R$ at160 K		Conductivity (S/cm) at 160 K			Conductivity (S/cm) at 295 K		
	C_{bulk}	C_{gb}	σ_{bulk}	σ_{gb}	σ_{total}	σ_{bulk}	σ_{gb}	σ_{total}
x = 0.0	$4.20 * 10^{-12}$	$47.30 * 10^{-9}$	$2.32 * 10^{-6}$	$8.75 * 10^{-7}$	$6.35 * 10^{-6}$	$1.30 * 10^{-3}$	$1.20 * 10^{-3}$	$6.32 * 10^{-4}$
x = 0.60	$2.34 * 10^{-12}$	$11.20 * 10^{-9}$	$7.35 * 10^{-7}$	$5.64 * 10^{-8}$	$1.00 * 10^{-7}$	$6.54 * 10^{-4}$	$1.39 * 10^{-4}$	$1.15 * 10^{-4}$

Acknowledgements

The authors would like to acknowledge the support of the Tertiary Education Trust Fund (TETFUND), Chemistry Department, University of Lagos, the University of Manchester and the Functional Materials and Devices Group at the Department of Materials Science and Engineering, University of Sheffield, United Kingdom.

Appendix A. Supporting information

Supplementary data associated with this article can be found in the online version at doi:10.1016/j.jeurceramsoc.2023.12.071.

References

[1] M.J. Burke, J.C. Stephens, Political power and renewable Energy futures: a critical review, Energy Res. Soc. Sci. 35 (2018) 78–93, https://doi.org/10.1016/j.erss.2017.10.018.
[2] V. Costantini, F. Gracceva, A. Markandya, G. Vicini, Security of energy supply: comparing scenarios from a European perspective, Energy Policy 35 (2007) 210–226, https://doi.org/10.1016/j.enpol.2005.11.002.
[3] A. Rudola, A.J.R. Rennie, R. Heap, S.S. Meysami, A. Lowbridge, F. Mazzali, R. Sayers, C.J. Wright, J. Barker, Commercialisation of high energy density sodium-ion batteries: Faradion's journey and outlook, J. Mater. Chem. A (2021), https://doi.org/10.1039/D1TA00376C.
[4] D. McNulty, A. Hennessy, M. Li, E. Armstrong, K.M. Ryan, A review of Li-ion batteries for autonomous mobile robots: perspectives and outlook for the future, J. Power Sources 545 (2022), 231943, https://doi.org/10.1016/j.jpowsour.2022.231943.
[5] E. Fan, L. Li, Z. Wang, J. Lin, Y. Huang, Y. Yao, R. Chen, F. Wu, Sustainable recycling technology for Li-ion batteries and beyond: challenges and future prospects, Chem. Rev. 120 (2020) 7020–7063, https://doi.org/10.1021/acs.chemrev.9b00535.
[6] M.K. Aslam, Y. Niu, T. Hussain, H. Tabassum, W. Tang, M. Xu, R. Ahuja, how to avoid dendrite formation in metal batteries: innovative strategies for dendrite suppression, Nano Energy 86 (2021), 106142, https://doi.org/10.1016/j.nanoen.2021.106142.
[7] H. Cha, J. Kim, Y. Lee, J. Cho, M. Park, Issues and challenges facing flexible lithium-ion batteries for practical application, Small 14 (2017) 1702989, https://doi.org/10.1002/smll.201702989.
[8] P.A. Christensen, P.A. Anderson, G.D.J. Harper, S.M. Lambert, W. Mrozik, M. A. Rajaeifar, M.S. Wise, O. Heidrich, Risk management over the life cycle of lithium-ion batteries in electric vehicles, Renew. Sustain. Energy Rev. 148 (2021), 111240, https://doi.org/10.1016/j.rser.2021.111240.
[9] H. Zhang, H. Zhao, M.A. Khan, W. Zou, J. Xu, L. Zhang, J. Zhang, Recent progress in advanced electrode materials, separators and electrolytes for lithium batteries, J. Mater. Chem. A 6 (2018) 20564–20620, https://doi.org/10.1039/c8ta05336g.
[10] K. Chayambuka, G. Mulder, D.L. Danilov, P.H.L. Notten, From Li-ion batteries toward Na-ion chemistries: challenges and opportunities, Adv. Energy Mater. 10 (2020), 2001310, https://doi.org/10.1002/aenm.202001310.
[11] Mauger, Julien, Paolella, Armand, Zaghib, Building better batteries in the solid state: a review, Materials 12 (2019) 3892, https://doi.org/10.3390/ma12233892.
[12] P. Jiang, G. Du, Y. Shi, F. She, P. Guo, G. Qian, X. Lu, F. Xie, X. Lu, Ultrafast sintering of $Na_3Zr_2Si_2PO_{12}$ solid electrolyte for long lifespan solid-state sodium-ion batteries, 138771–138771, Chem. Eng. J. 451 (2023), https://doi.org/10.1016/j.cej.2022.138771.
[13] J.F. Peters, A. Peña Cruz, M. Weil, Exploring the economic potential of sodium-ion batteries, Batteries 5 (2019) 10, https://doi.org/10.3390/batteries5010010.
[14] A.M. Bates, Y. Preger, L. Torres-Castro, K.L. Harrison, S.J. Harris, J. Hewson, Are solid-state batteries safer than lithium-ion batteries, Joule 6 (2022) 742–755, https://doi.org/10.1016/j.joule.2022.02.007.
[15] B. Xu, J. Lee, D. Kwon, L. Kong, M. Pecht, Mitigation strategies for Li-ion battery thermal runaway: a review, Renew. Sustain. Energy Rev. 150 (2021), 111437, https://doi.org/10.1016/j.rser.2021.111437.
[16] Y. Chen, Y. Kang, Y. Zhao, L. Wang, J. Liu, Y. Li, Z. Liang, X. He, X. Li, N. Tavajohi, B. Li, a review of lithium-ion battery safety concerns: the issues, strategies, and testing standards, J. Energy Chem. 59 (2021) 83–99, https://doi.org/10.1016/j.jechem.2020.10.017.
[17] D. Ouyang, M. Chen, Q. Huang, J. Weng, Z. Wang, J. Wang, A review on the thermal hazards of the lithium-ion battery and the corresponding countermeasures, Appl. Sci. 9 (2019) 2483, https://doi.org/10.3390/app9122483.
[18] D.H.S. Tan, A. Banerjee, Z. Chen, Y.S. Meng, From nanoscale interface characterisation to sustainable energy storage using all-solid-state batteries, Nat. Nanotechnol. 15 (2020) 170–180, https://doi.org/10.1038/s41565-020-0657-x.
[19] Y. Tian, G. Zeng, A. Rutt, T. Shi, H. Kim, J. Wang, J. Koettgen, Y. Sun, B. Ouyang, T. Chen, Z. Lun, Z. Rong, K. Persson, G. Ceder, Promises and challenges of next-generation "beyond Li-ion" batteries for electric vehicles and grid decarbonization, Chem. Rev. 121 (2020) 1623–1669, https://doi.org/10.1021/acs.chemrev.0c00767.
[20] M. Semadeni, Energy storage as an essential part of sustainable energy systems, RePEc: Res. Pap. Econ. 24 (2003), https://doi.org/10.3929/ethz-a-004532521.
[21] S.Y. Hong, Y. Kim, Y. Park, A. Choi, N.-S. Choi, K.T. Lee, Charge carriers in rechargeable batteries: Na ions vs Li ions, Energy Environ. Sci. 6 (2013) 2067, https://doi.org/10.1039/c3ee40811f.
[22] Y. Yu, H. Xu, Z. Wang, G. Shao, Transport of sodium ions in solids: progress in first-principle theoretical formulation of potential solid sodium-ion electrolytes, Batter. Supercaps 4 (2021) 1096–1107, https://doi.org/10.1002/batt.202000320.
[23] F. Wu, K. Zhang, Y. Liu, H. Gao, Y. Bai, X. Wang, C. Wu, Polymer electrolytes and interfaces toward solid-state batteries: Recent advances and prospects, Energy Storage Mater. 33 (2020) 26–54, https://doi.org/10.1016/j.ensm.2020.08.002.
[24] W. Zhang, C. Zhao, X. Wu, Research progresses on interfaces in solid-state sodium batteries: a topic review, Adv. Mater. Interfaces 7 (2020), https://doi.org/10.1002/admi.202001444.
[25] Y. Huang, B. Shao, F. Han, Interfacial challenges in all-solid-state lithium batteries, Curr. Opin. Electrochem. 33 (2022), 100933, https://doi.org/10.1016/j.coelec.2021.100933.
[26] S. Gandi, V.S. Chidambara Swamy Vaddadi, S.S. Sripada Panda, N.K. Goona, S. R. Parne, M. Lakavat, A. Bhaumik, Recent progress in the development of glass and glass-ceramic cathode/solid electrolyte materials for next-generation high capacity all-solid-state sodium-ion batteries: A review, J. Power Sources 521 (2022), 230930, https://doi.org/10.1016/j.jpowsour.2021.230930.
[27] C. Zhou, S. Bag, Venkataraman Thangadurai, Engineering materials for progressive all-solid-state Na batteries, ACS Energy Lett. 3 (2018) 2181–2198, https://doi.org/10.1021/acsenergylett.8b00948.
[28] J.A.S. Oh, L. He, B. Chua, K. Zeng, L. Lu, Inorganic sodium solid-state electrolyte and interface with sodium metal for room-temperature metal solid-state batteries, Energy Storage Mater. 34 (2021) 28–44, https://doi.org/10.1016/j.ensm.2020.08.037.
[29] E. Matios, H. Wang, W. Li, Interface Engineering on Solid-State Ceramic Electrolyte by Graphene-like Coating for Electrochemically Stable Sodium Metal Batteries, ECS Meeting Abstracts. MA2019–01 (2019) 152–152. 〈https://doi.org/10.1149/ma2019–01/2/152〉.
[30] Y. Lu, L. Li, Q. Zhang, Z. Niu, J. Chen, Electrolyte and interface engineering for solid-state sodium batteries, Joule 2 (2018) 1747–1770, https://doi.org/10.1016/j.joule.2018.07.028.
[31] M.V. Reddy, C.M. Julien, A. Mauger, K. Zaghib, Sulfide and oxide inorganic solid electrolytes for all-solid-state Li batteries: a review, Nanomaterials 10 (2020) 1606, https://doi.org/10.3390/nano10081606.
[32] S. Teng, J. Tan, A. Tiwari, Recent developments in garnet-based solid-state electrolytes for thin film batteries, Curr. Opin. Solid State Mater. Sci. 18 (2014) 29–38, https://doi.org/10.1016/j.cossms.2013.10.002.
[33] J.B. Bates, J. Wang, N.J. Dudney, Solid electrolytes-the beta aluminas, Phys. Today 35 (1982) 46–53, https://doi.org/10.1063/1.2915170.
[34] Y. Wang, Y. Wu, Z. Wang, L. Chen, H. Li, F. Wu, Doping strategy and mechanism for oxide and sulfide solid electrolytes with high ionic conductivity, J. Mater. Chem. A 10 (2022) 4517–4532, https://doi.org/10.1039/D1TA10966A.
[35] Y. Chen, K. Wen, T. Chen, X.-J. Zhang, M. Armand, S. Chen, Recent progress in all-solid-state lithium batteries: the emerging strategies for advanced electrolytes and their interfaces 31 (2020) 401–433, https://doi.org/10.1016/j.ensm.2020.05.019.
[36] H.-L. Yang, B.-W. Zhang, K. Konstantinov, Y.-X. Wang, H.-K. Liu, S.-X. Dou, Progress and challenges for all-solid-state sodium batteries, Adv. Energy Sustain. Res. 2 (2021), 2000057, https://doi.org/10.1002/aesr.202000057.
[37] S. Jian, Y. Cao, W. Feng, G. Yin, Y. Zhao, Y. Lai, T. Zhang, X. Li, H. Wu, H. Bi, Y. Dong, Recent progress in solid polymer electrolytes with various dimensional fillers: a review, 100224–100224, Mater. Today Sustain. 20 (2022), https://doi.org/10.1016/j.mtsust.2022.100224.
[38] M. Avdeev, Crystal chemistry of NASICONs: ideal framework, distortion, and connection to properties, Chem. Mater. 33 (2021) 7620–7632, https://doi.org/10.1021/acs.chemmater.1c02695.
[39] R. Rajagopalan, Z. Zhang, Y. Tang, C. Jia, X. Ji, H. Wang, Understanding crystal structures, ion diffusion mechanisms and sodium storage behaviours of NASICON

materials, Energy Storage Mater. 34 (2021) 171–193, https://doi.org/10.1016/j.ensm.2020.09.007.

[40] L. Ran, Ardeshir Baktash, M. Li, Y. Yin, B. Demir, T. Lin, M. Li, M. Rana, I.R. Gentle, L. Wang, D.J. Searles, R. Knibbe, Sc, Ge co-doping NASICON boosts solid-state sodium ion batteries' performance, Energy Storage Mater. 40 (2021) 282–291, https://doi.org/10.1016/j.ensm.2021.05.017.

[41] D.A. Edelman, T.G. Brandt, E. Temeche, R.M. Laine, Sodium-based solid electrolytes and interfacial stability. Towards solid-state sodium batteries, Mater. Today Commun. 32 (2022), 104009, https://doi.org/10.1016/j.mtcomm.2022.104009.

[42] A. Parejiya, R. Essehli, R. Amin, J. Liu, N. Muralidharan, H.M. Meyer, D.L. Wood, I. Belharouak, $Na_{1+x}Mn_{x/2}Zr_{2-x/2}(PO_4)_3$ as a Li^+ and Na^+ super ion conductor for solid-state batteries, ACS Energy Lett. 6 (2021) 429–436, https://doi.org/10.1021/acsenergylett.0c02513.

[43] Z. Deng, G. Sai Gautam, S.K. Kolli, J.-N. Chotard, A.K. Cheetham, C. Masquelier, P. Canepa, Phase behavior in rhombohedral NASICON electrolytes and electrodes, Chem. Mater. 32 (2020) 7908–7920, https://doi.org/10.1021/acs.chemmater.0c02695.

[44] M. Samiee, B. Radhakrishnan, Z. Rice, Z. Deng, Y.S. Meng, S.P. Ong, J. Luo, Divalent-doped $Na_3Zr_2Si_2PO_{12}$ natrium superionic conductor: Improving the ionic conductivity via simultaneously optimising the phase and chemistry of the primary and secondary phases, J. Power Sources 347 (2017) 229–237, https://doi.org/10.1016/j.jpowsour.2017.02.042.

[45] P. Yadav, M.C. Bhatnagar, Structural studies of NASICON material of different compositions by sol–gel method, Ceram. Int. 38 (2012) 1731–1735, https://doi.org/10.1016/j.ceramint.2011.09.022.

[46] A. Ignaszak, P. Pasierb, R. Gajerski, S. Komornicki, Synthesis and properties of Nasicon-type materials, Thermochim. Acta 426 (2005) 7–14, https://doi.org/10.1016/j.tca.2004.07.002.

[47] A. Jalalian-Khakshour, C.O. Phillips, L. Jackson, T.O. Dunlop, S. Margadonna, D. Deganello, Solid-state synthesis of NASICON ($Na_3Zr_2Si_2PO_{12}$) using nanoparticle precursors for optimisation of ionic conductivity, J. Mater. Sci. 55 (2019) 2291–2302, https://doi.org/10.1007/s10853-019-04162-8.

[48] S.K. Pal, R. Saha, G.V. Kumar, S. Omar, Designing high ionic conducting NASICON-type $Na_3Zr_2Si_2PO_{12}$ solid-electrolytes for Na-ion batteries, J. Phys. Chem. C. 124 (2020) 9161–9169, https://doi.org/10.1021/acs.jpcc.0c00543.

[49] J.-S. Lee, C.-M. Chang, Y.I. Lee, J.-H. Lee, S.-H. Hong, Spark plasma sintering (SPS) of NASICON ceramics, J. Am. Ceram. Soc. 87 (2004) 305–307, https://doi.org/10.1111/j.1551-2916.2004.00305.x.

[50] K. Okubo, H. Wang, K. Hayashi, M. Inada, N. Enomoto, G. Hasegawa, T. Osawa, H. Takamura, A dense NASICON sheet prepared by tape-casting and low-temperature sintering, Electrochim. Acta 278 (2018) 176–181, https://doi.org/10.1016/j.electacta.2018.05.020.

[51] S. Naqash, Q. Ma, F. Tietz, O. Guillon, $Na_3Zr_2(SiO_4)_2(PO_4)$ prepared by a solution-assisted solid-state reaction, Solid State Ion. 302 (2017) 83–91, https://doi.org/10.1016/j.ssi.2016.11.004.

[52] H. Leng, J. Huang, J. Nie, J. Luo, Cold sintering and ionic conductivities of $Na_{3.256}Mg_{0.128}Zr_{1.872}Si_2PO_{12}$ solid electrolytes, J. Power Sources 391 (2018) 170–179, https://doi.org/10.1016/j.jpowsour.2018.04.067.

[53] A. Chakraborty, Raghunayakula Thirupathi, S. Bhattacharyya, K. Singh, S. Omar, Mg-doped NASICON-type electrolyte for rechargeable solid-state sodium-ion batteries, 233092-233092 572 (2023), https://doi.org/10.1016/j.jpowsour.2023.233092.

[54] Y.B. Rao, L.N. Patro, Influence of synthesis methodology and excess Na on the ionic transport properties of natrium superionic conductor, $Na_3Zr_2Si_2PO_{12}$, Mater. Lett. 301 (2021), 130267, https://doi.org/10.1016/j.matlet.2021.130267.

[55] M. Barj, G. Lucazeau, C. Delmas, Raman and infrared spectra of some chromium NASICON-type materials: short-range disorder characterisation, J. Solid State Chem. 100 (1992) 141–150, https://doi.org/10.1016/0022-4596(92)90164-q.

[56] K. Ren, Y. Cao, Y. Chen, G. Shao, J. Dai, Y. Wang, Flash sintering of $Na_3Zr_2(SiO_4)_2(PO_4)$ solid-state electrolyte at furnace temperature of 700 °C, Scr. Mater. 187 (2020) 384–389, https://doi.org/10.1016/j.scriptamat.2020.06.055.